Journal of Vacuum Science & Technology B
ACCEPTED MANUSCRIPT

PLEASE CITE THIS ARTICLE AS DOI: 10.1116/6.0005158

On the Contrast Mechanism of Scanning Microwave Impedance Microscopy on Buried and Doped Features

Lorenzo Andrea Magnarin[1,2], Filippo Ozino Caligaris[1], José Morán-Meza[3], Jasmin Aghassi-Hagmann[2], and Umberto Celano[1,a)]

[1]School of Electrical, Computer, and Energy Engineering, Arizona State University, 650 E. Tyler Mall, Tempe, Arizona 85281, USA

[2]Karlsruhe Institute of Technology (KIT), Kaiserstraße 12, 76131 Karlsruhe, Germany

[3]Laboratoire national de métrologie et d'essais (LNE), Avenue Roger Hennequin 29, 78197 Trappes Cedex, France

a)Author to whom correspondence should be addressed: umberto.celano@asu.edu

Abstract – This work investigates the contrast mechanisms that govern scanning microwave impedance microscopy (sMIM) when applied to the characterization of advanced semiconductor devices. Systematic experiments were performed to evaluate how parameters such as tip–sample interaction, microwave excitation, and environmental conditions influence the sMIM response. The results provide insight into the relative contributions of dielectric and conductive components to the measured signal, clarifying the conditions that optimize imaging sensitivity and stability. Measurements on reference samples with buried oxide patterns and dopant calibration structures confirm sMIM's ability to resolve nanoscale electrical variations beneath the surface. The study establishes sMIM as a powerful, non-destructive technique for mapping local electrical properties in three-dimensional and buried

device architectures. These findings emphasize its relevance for semiconductor failure analysis, process monitoring, and future metrology standards development.

I. INTRODUCTION

The rapid progress in semiconductor technology continues to increase the demand for more advanced metrology and characterization techniques.[1] New device architectures, such as Gate-All-Around Field-Effect Transistors (GAAFETs) and Complementary Field-Effect Transistors (CFETs), depend on intricate three-dimensional structures to sustain performance scaling and follow the industry's ongoing miniaturization goals.[2,3] These technological advances, while enabling improved electrostatic control and reduced leakage currents, also introduce substantial challenges for conventional characterization techniques, such as conductive atomic force microscopy (C-AFM), scanning spreading resistance microscopy (SSRM), and scanning capacitance microscopy (SCM), which often lack the spatial resolution or sensitivity required to probe electrical properties of three-dimensional nanoscale materials. In particular, upcoming transistor architectures such as the GAA pose significant difficulties for assessing dopant activation, junction profiling, monitoring epitaxial growth in the source and drain regions, detecting void formation, and mapping strain distributions, among other parameters.[4–6] Previous reports discussed the complexity of the analysis for critical manufacturing steps such as wire release, spacer uniformity, cavity etch, and junction activation.[7–9] Among emerging nanoscale characterization techniques, microwave-based and near-field-assisted scanning probe methods, such as scanning microwave impedance microscopy (sMIM), have demonstrated significant promise in addressing the limitations of conventional methods.[10,11]

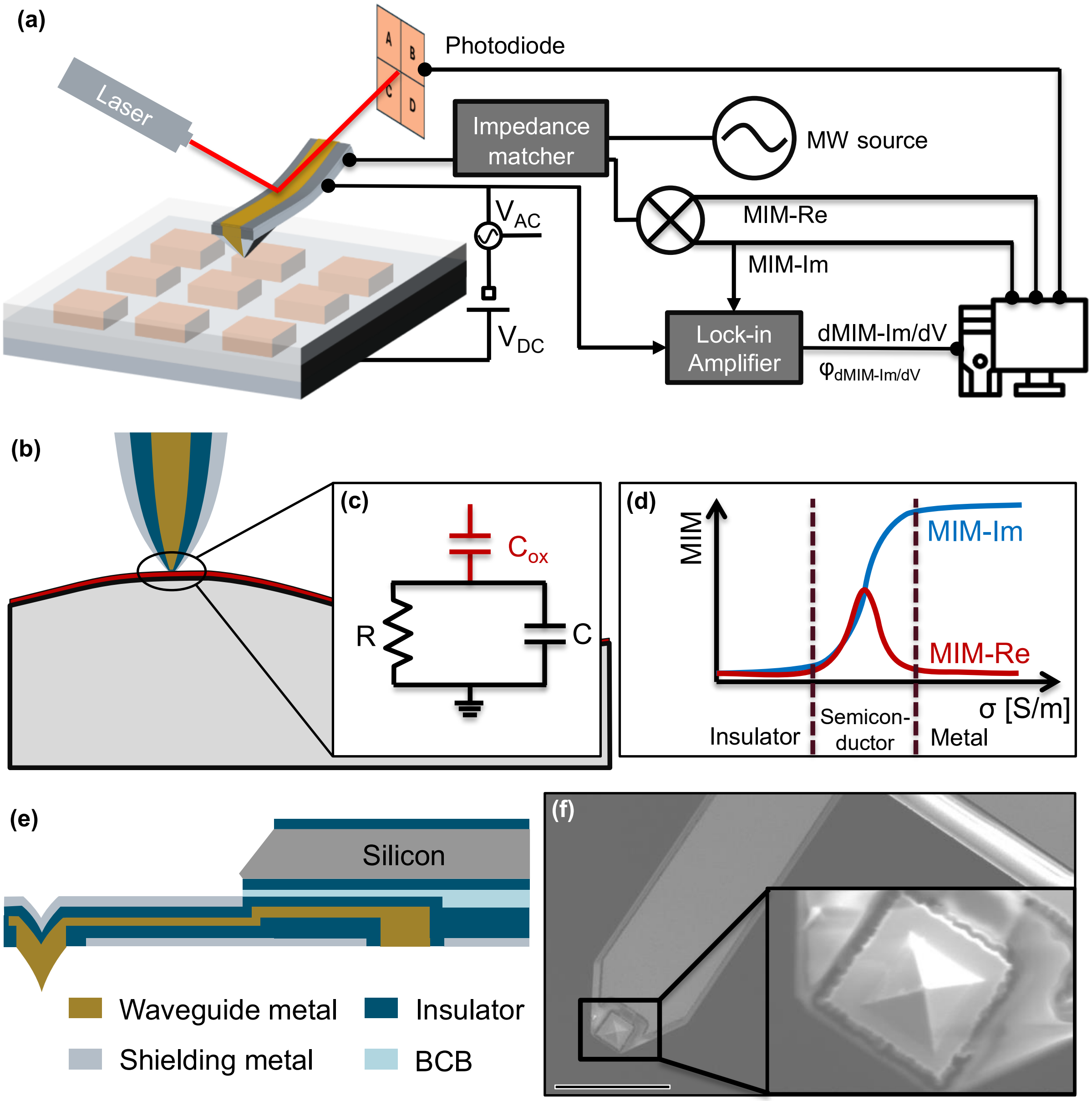

Figure 1: (a) Schematic representation of an sMIM setup. (b) Diagram of the tip-sample interaction, considering a thin surface oxide layer. (c) Equivalent circuit of the tip-sample impedance with lumped elements simplification. (d) Characteristic MIM-Im (MIM-C) and MIM-Re (MIM-R) response to features of varying conductivity. (e) Schematic representation of an sMIM shielded probe. (f) SEM image of a PrimeNano 150 µm probe (scalebar: 50 µm).

Transmitting a microwave signal through a shielded cantilever-tip assembly enables simultaneous mapping of local resistive and capacitive properties with nanometer-scale resolution. Its sensitivity to variations in permittivity and conductivity, coupled with the deep microwave interaction volume, makes it particularly effective for probing subsurface electrical features, dopant distributions, and buried interfaces in semiconductor devices.[12] Owing to this versatility, sMIM has been successfully applied to a broad range of systems, including advanced transistor architectures,[13] two-dimensional materials,[14–16] ferroelectric materials,[17] and dielectric heterostructures.[18] The integration of microwave excitation with scanning probe microscopy has demonstrated significant utility in a range of applications, particularly for the detection and characterization of buried features and for the quantitative assessment of dopant concentrations in semiconductor structures.[19] Despite its growing adoption, the mechanisms underlying sMIM signal contrast generation remain only partially understood, particularly for complex and buried structures.[20] This work reports on a dedicated design of experiments to clarify the understanding of sMIM contrast formation by systematically investigating the influence of key experimental parameters relevant to modern semiconductor device characterization.

II. MATERIALS AND METHODS

A. Scanning Microwave Impedance Microscopy (sMIM)

Measurements were performed using a commercial sMIM module (PrimeNano Inc.) integrated with an NX-Hivac atomic force microscope (Park Systems). The setup comprises dedicated electronics for microwave signal generation, coupling, and demodulation, as schematically shown in Figure **1a**. To ensure efficient signal transfer and minimize reflection losses, a 50 Ω impedance-matching network is also included between the probe and the microwave source. The reflected microwave signal was demodulated and recorded using the ScanWave Pro software (PrimeNano), yielding capacitive and resistive components, hereafter referred to as MIM-C and MIM-R, respectively. For differential measurements, the signals were further processed using a lock-in detection scheme in which a small a.c. bias voltage was applied to the probe. This configuration enables the extraction of the differential capacitance (dC/dV amplitude and phase), analogous to the detection principle used in SCM, as previously reported.[13,21–23] Signal contrast originates from the interaction between the near-field microwave probing volume and the local electrical environment of the sample. This interaction can be described by a lumped-element equivalent circuit, where the tip–sample admittance is expressed as

$$Y_{ts} = \frac{1}{Z_{ts}} = G + j\omega C_{\text{eff}}, \tag{1}$$

with G representing the local conductance and C_{eff} the effective capacitance. In most semiconductor samples, a thin native oxide layer introduces an additional dielectric contribution, modeled as a series capacitance (Figures **1b,c**). The dependence of the MIM-C and MIM-R responses on material conductivity is summarized in Figure **1d**. In insulating materials, deep field penetration produces weak signals in both channels. In semiconductors, partial field screening enhances the capacitive response and introduces dielectric losses, whereas in metals, complete screening results in a saturated MIM-C and a diminished MIM-R signal.[24] To minimize parasitic capacitance and improve measurement fidelity, shielded cantilever probes were employed (PrimeNano sMIM-150). These probes feature a metallic waveguide enclosed between two shielding layers separated by an insulating film (Figure **1e**).[25] The pyramidal geometry of the tip is shown in the SEM image in Figure **1f**.

B. *Buried oxide reference sample*

To investigate the response of the technique to buried dielectric structures, an aspect of particular importance for advanced semiconductor metrology, a buried-oxide reference sample was employed. The specimen consists of an array of 5 x 5 μm^2 SiO_2 squares embedded beneath

Journal of Vacuum Science & Technology B

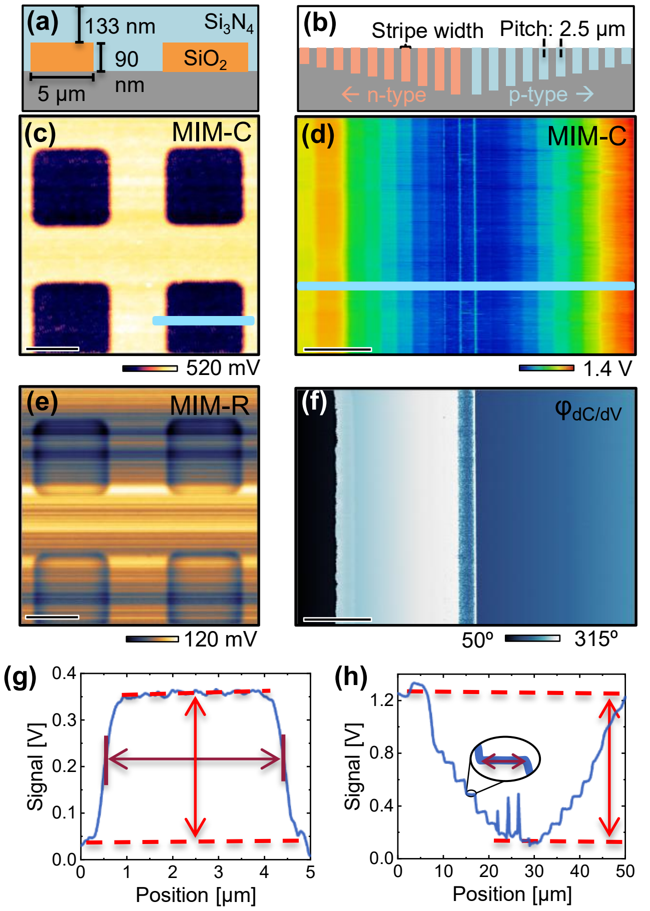

Figure 2: (a) Schematic representation of the buried oxide sample. (b) Schematic representation of the Infineon dopant calibration sample. (c) and (e) MIM-C and MIM-R channel of the buried oxide sample (scalebar: 5µm). (d) and (f) MIM-C and $\phi_{dC/dV}$ channel of the 2 µm width stripes of the Infineon sample (scalebar: 10 µm). (g) Profile extracted from (c) (yellow line) with dynamic range (bright red) and FWHM (dark red) metrics overlayed on the profile. (h) Profile extracted from (d) (yellow line) with the same metrics overlayed on the profile.

a 133 nm-thick Si_3N_4 overlayer, as schematically illustrated in Figure **2a**. The 90 nm-thick SiO_2 regions were thermally grown on a silicon substrate, followed by deposition of a Si_3N_4 layer and subsequent chemical–mechanical polishing (CMP) to achieve a planar surface and a controlled residual thickness above the buried oxide features. During imaging, the buried SiO_2 regions produced the most pronounced contrast in the capacitive channel (MIM-C), as shown in Figure **2c**, while the resistive channel (MIM-R) exhibited a response ca. 20 times weaker (Figure **2e**). The striated pattern visible in Figure **2e** is deemed as an artifact which arises from the very low signal-to-noise ratio of the MIM-R channel on purely capacitive samples in combination with the raster-scan nature of AFM-based modes. Owing to the dominant capacitive contrast associated with the oxide features, the MIM-C signal was selected as the primary metric for further analysis and interpretation.

C. *Dopant calibration reference sample*

To assess the response of the technique to electrically active dopants, a dopant calibration sample supplied by Infineon Technologies AG was utilized. The specimen comprises ten n-type and ten p-type implanted stripes with systematically varied doping concentrations, as schematically shown in Figure **2b**. The higher level of penetration into the sample, typical of microwaves, and the use of a planar calibration sample, rather than a cross-sectioned sample that requires cleaving and polishing, minimizes the influence of unwanted sample morphology on the sMIM signal.[26] Controlled carrier densities were achieved through ion implantation, and secondary ion mass spectrometry (SIMS) data provided by Infineon Technologies AG confirmed a uniform dopant distribution within the upper 200 nm of the surface region. The implanted stripes display widths of 0.5 µm, 1.0 µm, and 2.0 µm, arranged with a periodic pitch of 2.5 µm. Imaging of the 2.0 µm-wide stripe region revealed a clear alternating contrast in the capacitive channel (MIM-C), corresponding to the periodic sequence of n-type and p-type regions (Figure **2d**). The differential capacitance phase signal (dC/dV phase), presented in Figure **2f**, further distinguishes the dopant polarity, with n-type regions appearing on the left side of the staircase-like profile and p-type regions on the right. These observations demonstrate the capability of the technique to resolve both the spatial distribution and electrical polarity of doped semiconductor structures with sub-micrometer precision.

D. *Figures of Merit*

For a consistent comparison between measurements obtained from both reference samples and to clarify the underlying contrast mechanisms, identical quantitative metrics were evaluated. Two figures of merit were defined: the dynamic range and the full width at half maximum

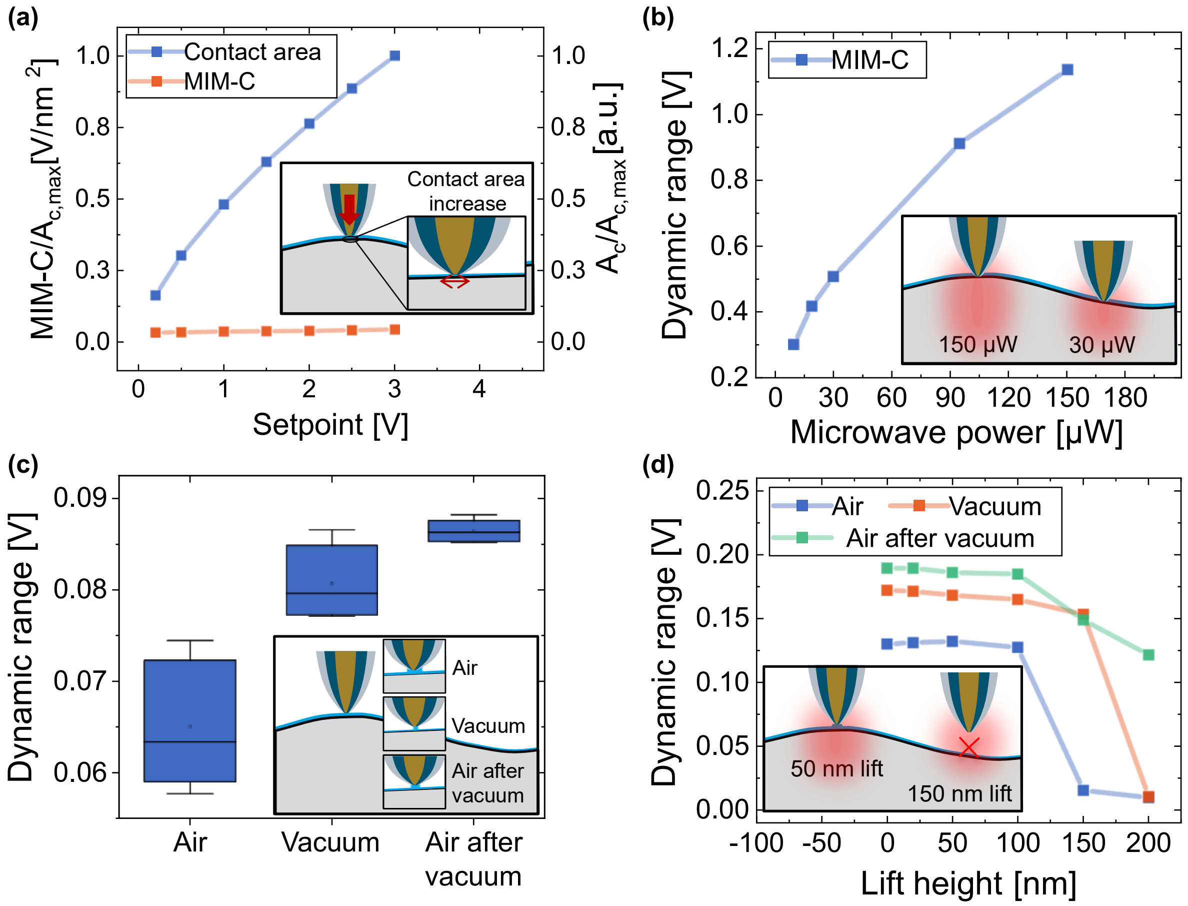

Figure 3: (a) MIM-C dynamic range dependence on tip-sample pressure (red) compared to the tip-sample contact area scaling for increasing tip-sample pressure according to the Hertz model (blue). Conversion factor after thermal tuning of the probe: 1.04 nN/V. Inset: variation of tip-sample contact area for increased setpoint value (tip-sample pressure). (b) MIM-C dynamic range dependence on microwave power shows an almost linear trend. Setpoint: 1.0 V. Inset: possible variation of the microwave interaction volume with an increase in power. (c) MIM-C dynamic range of several sMIM measurements in three different AFM chamber environments: air, high-vacuum (~7e-5 mbar), and air after vacuum. Inset: possible variation of the water meniscus forming between the tip and the sample for the different environments. (d) MIM-C dynamic range dependence on the tip height in lift mode measurements in air (blue), vacuum (red), and air after vacuum (green). Microwave power: 30 μW. Inset: possible role of the water meniscus for microwave coupling.

(FWHM). The dynamic range corresponds to the voltage difference between the minimum and maximum signal values along a cross-sectional profile, providing a measure of the signal variation, which occurs at the transition between Si_3N_4 and buried SiO_2 features during the scan. The FWHM denotes the lateral distance between the two midpoint locations on a rising or falling signal edge and serves as an indicator of spatial resolution. The signal's edges are considered as the transition points between Si_3N_4 and SiO_2. A large dynamic range enhances the detectability of weakly contrasting or buried features, while the FWHM provides insight into the lateral probing volume and the effective resolution limit of the technique.

Representative cross-sectional profiles extracted from the yellow line overlayed in Figures **2c** and **2d**, showing the identified dynamic range (highlighted in bright red) and FWHM (highlighted in dark red), are presented in Figures **2g** and **2h**.

E. SCM and SSRM

Scanning capacitance microscopy (SCM) and scanning spreading resistance microscopy (SSRM) measurements were carried out using the respective modules of a Bruker Dimension Icon atomic force microscope. SCM measurements employed conventional Bruker PtIr-coated probes (SCM-PIT-v2) and were performed at 75 kHz. In contrast, SSRM measurements were performed using full diamond tip (FDT) probes supplied by imec and were performed at a high tip-sample pressure (setpoint of 5 V). SCM and sMIM rely on fundamentally different contrast mechanisms. In SCM, the signal corresponds to the local differential capacitance (dC/dV) of the nano-MOS structure formed under the tip and is therefore strongly dependent on carrier depletion and accumulation induced by the applied DC bias. In contrast, sMIM probes the local electrical response without requiring bias-induced carrier modulation, leading to differences in sensitivity, noise characteristics, and bias dependence between the two modes.

III. RESULTS

In this study, a series of experimental parameters was systematically varied to elucidate the contrast mechanisms in sMIM. As a first step, the dependence of measurement sensitivity on tip-sample pressure was examined using the dynamic range as a figure of merit. In several SPM techniques based on two-probe experiments, such as C-AFM and SSRM, an increase in tip-sample contact pressure corresponds to an increase in measured current due to the enlargement of the electrical contact area. However, in sMIM measurements of the buried oxide reference sample, when both the MIM-C dynamic range and the estimated tip-sample contact area are plotted as a function of the setpoint, which is the control parameter used to adjust the applied tip–sample force, markedly different trends emerge, as illustrated in Figure **3a**. Here, for the sake of simplicity, the contact area is estimated using the Hertzian contact model, which relates the effective (assumed circular) contact radius a, and therefore the contact area A, to the normal force exerted by the tip on the sample surface:

$$a = \left(\frac{3 \times \left(1.04\frac{nN}{V} \times V_{sp}\right) \times R}{4 \times E^{*}}\right)^{1/3} \Rightarrow A = \pi a^{2} = \pi \left(\frac{3.12 \times V_{sp} \times R}{4E^{*}}\right)^{2/3}, \tag{2}$$

where V_{sp} is the setpoint in volts, 1.04 nN/V is the conversion factor between setpoint (in volts) and force (in nN), R is the nominal tip radius (50 nm according to the vendor), and E^{*} is the Young's modulus of the sample's surface material, in this case Si_3N_4. Within the investigated setpoint range of 0.2 V to 3.0 V, the estimated tip–sample contact area increases substantially; however, the MIM-C dynamic range remains essentially unchanged. In contrast, the sensitivity of the MIM-C channel exhibits a strong dependence on the applied microwave power. Figure **3b** presents the MIM-C dynamic range extracted from sMIM measurements of the buried oxide reference sample as a function of microwave power, varied between 5 µW and 150 µW. The observed trend is nearly linear, indicating that higher microwave power enhances the sensitivity of sMIM to subsurface features. A similar behavior is observed for doped structures, such as those in the Infineon dopant calibration sample (data not shown). Owing to the integration of our sMIM system with a high-vacuum atomic force microscope, we were able to investigate the influence of the water meniscus on the measurement contrast in greater detail, which is a factor frequently discussed in the sMIM literature.[12,27–29] Multiple works using finite element modeling (FEM) simulations suggest that the water meniscus formed between the probe and the sample enhances microwave coupling, thereby increasing both signal intensity and overall sensitivity. Although complete removal of adsorbed water cannot be achieved even under high vacuum, the residual water layer is expected to be significantly thinner, resulting in a smaller meniscus. Dynamic range measurements performed under high vacuum conditions (7×10^{-7}

mbar) revealed higher sensitivity compared to measurements in ambient air (Figure **3c**). While this improvement cannot be solely attributed to the reduction of the water meniscus, it likely represents one of the dominant contributing factors. Interestingly, a further enhancement in dynamic range was observed when ambient air was reintroduced into the chamber, and measurements were repeated immediately at atmospheric pressure. These effects were consistently reproducible, independent of the probe, sample, or measurement day. During transitions between environments, the tip was retracted 1 μm from the sample surface and re-engaged prior to measurement to prevent tip damage during pumping and flooding. All experiments were performed on the same day, at the same location on the sample, and using the same probe. This phenomenon was observed to last for up to 16 hours. Additional experiments demonstrated that cycling between air and vacuum conditions produced a beneficial effect on the signal dynamic range, both when only the probe and when only the sample were exposed to high vacuum conditions. In essence, we separated the contribution of each element to understand the key factor driving the enhancement in the signal. This observation implies that the underlying physical mechanism responsible for the enhancement manifests in both components (see Figure **S1**). In addition, to further explore this behavior, sMIM measurements were also performed in lift mode, wherein the probe first scans the surface in contact and is then retracted to a fixed height following the sample topography. Here, the rationale is to push the tip-sample junction into a configuration where the role of the water meniscus could be emphasized by the progressive opening of a gap in the tip-sample junction.

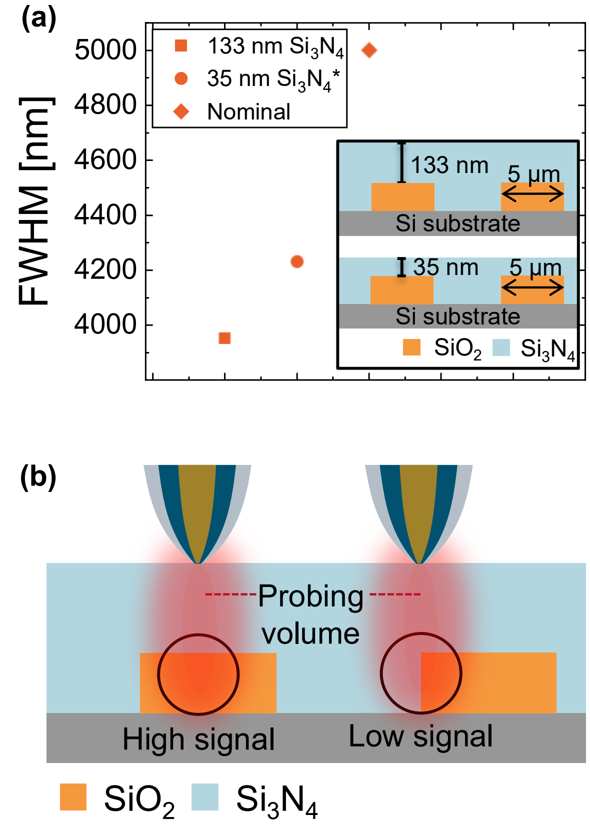

Figure 4: (a) Measured feature size of SiO2 features buried underneath 133 nm and 35 nm of Si_3N_4 compared to the nominal feature size of 5000 nm. *From Rubin et al. Inset: Schematic representation of the two different buried oxide samples. (b) The large size of the microwave interaction volume could explain the undersampling phenomenon visible for buried features.*

The dependence of the MIM-C dynamic range on lift height for all three environmental conditions is presented in Figure **3d**. The data confirms that the dynamic range increases in vacuum and further improves upon re-exposure to air after vacuum cycling. For all environments, a distinct tip-sample distance threshold was observed beyond which the dynamic range decreased sharply. Notably, the vacuum measurements exhibited a delayed loss of signal, suggesting a prolonged influence of the water meniscus on tip adhesion.

In addition to sensitivity, the lateral resolution of sMIM was evaluated by analyzing the variation of the FWHM figure of merit under the parameter changes described in the previous section. Measurements performed on the buried oxide reference sample exhibited a pronounced underestimation of the patterned features, yielding an average measured feature width of 3955

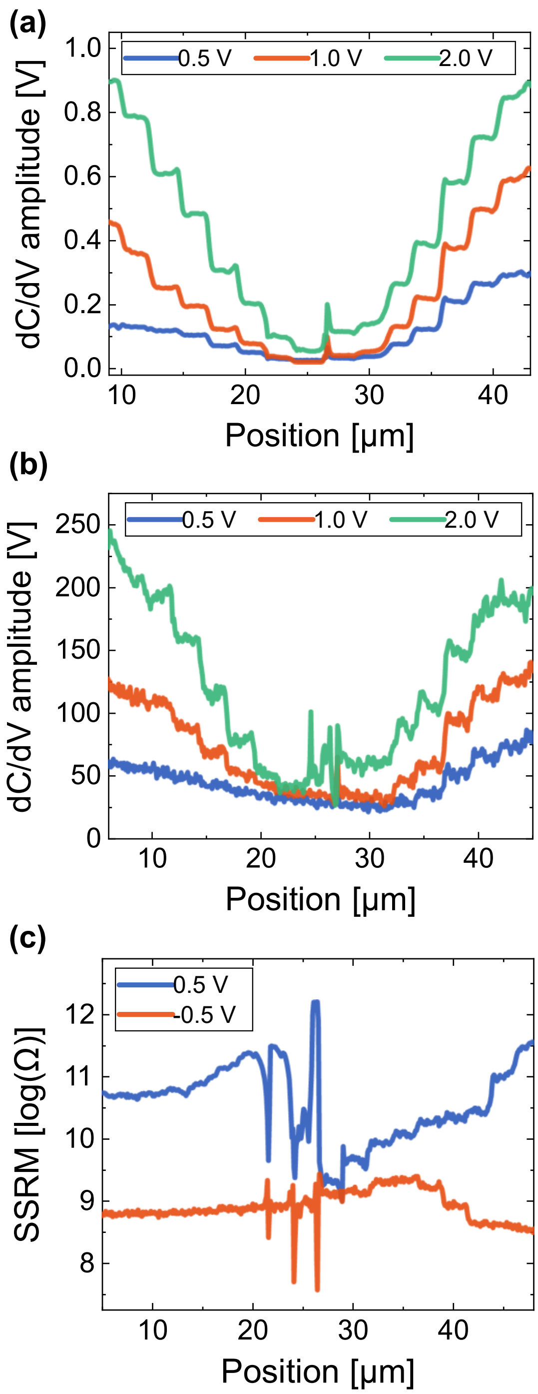

Figure 5: (a) dC/dV amplitude profiles extracted from sMIM measurements on the Infineon Dopant Calibration sample (2 µm stripe width) acquired at different lock-in modulating a.c. bias values (+0.5 V, blue, +1.0 V, red, and +2.0 V, green). (b) Analogous profiles to (a) extracted from SCM measurements at the same lock-in modulating a.c. bias values. (c) Spreading resistance profiles extracted from SSRM measurements on the Infineon Dopant Calibration sample (2 µm stripe width) acquired at different d.c. bias values (+0.5 V, blue, and -0.5 V, red).

± 20 nm compared to the nominal 5000 nm, as can be seen in Figure **4a**. For comparison, previously reported measurements acquired using the same sMIM system on an earlier version of the sample, with a thinner Si_3N_4 capping layer of 35 nm (as opposed to 133 nm in the present study), showed a measured feature width of 4232 nm.[16] This observation indicates that the depth of the buried structures significantly influences the ability of sMIM to resolve them accurately. This observation also suggests that the effective microwave probing volume contracts with increasing probing depth, such that a detectable signal is obtained only when a substantial portion of the buried feature lies within this volume, thereby leading to an apparent reduction in the measured feature size (see Figure **4b**). Variations in tip-sample pressure and applied microwave power did not produce any appreciable change in the measured feature width (data not shown), which implies a non-dependency of sMIM's spatial resolution on the aforementioned parameters.

The three-dimensional architectures of next-generation transistor devices comprise both heavily and lightly doped regions, increasing the demand for nanoscale techniques capable of sub-surface dopant characterization. Among scanning probe methods, SCM, SSRM, and sMIM currently constitute the principal characterization techniques used for dopant calibration, each positioning itself differently depending on measurement needs.[30] While SCM remains the most widely employed technique for active dopant profiling, its sensitivity is largely confined to near-surface regions owing to the relatively low frequency of the a.c. excitation used to modulate charge carriers. In contrast, sMIM enables probing of electrically active dopants at greater depths, owing to its operation at gigahertz frequencies (~3 GHz). Figures **5a–c** present results obtained from sMIM, SCM, and SSRM measurements on the Infineon Dopant Calibration sample. For both sMIM and SCM, data were acquired at a.c. modulation amplitudes of 0.5 V (blue), 1.0 V (red), and 2.0 V (green) to assess the response of the signal to increasing excitation bias. In both techniques, the signal intensity increases with a.c. bias; however, sMIM exhibits more clearly defined dopant terraces and substantially lower noise across the doped

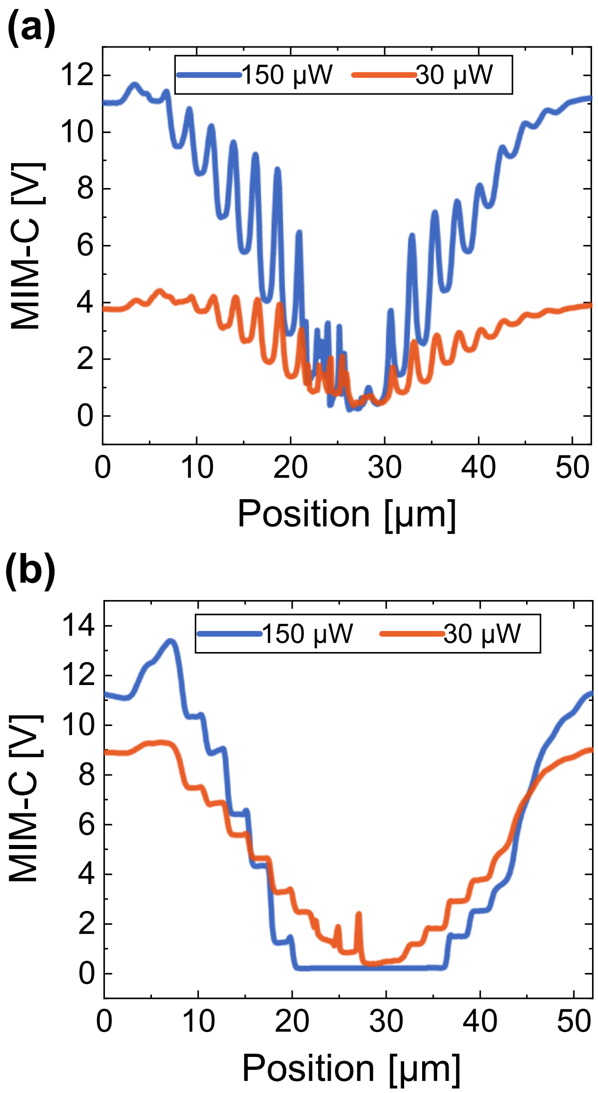

Figure 6: (a) MIM-C profiles extracted from sMIM measurements on the Infineon Dopant Calibration sample (1 µm stripe width) and (b) (2 µm stripe width) at two different microwave power values (150 µW, blue, and 30 µW, red).

stripes, which is in accordance with other studies comparing SCM with sMIM.[31] Moreover, sMIM profiles demonstrate a higher signal-to-noise ratio (SNR) and reduced asymmetry between n-type and p-type regions. This asymmetry in the SCM signal is typical of Metal-Oxide-Semiconductor structures such as the one used during this work and is caused by a mismatch in flatband voltage between p- and n-type structures.[32,33] The latter contrast asymmetry is clearly visible in the SSRM profiles (Figure **5c**), acquired under both positive (blue) and negative (red) d.c. bias. This behavior likely arises from the absence of an electrical back contact combined with the p-type silicon substrate of the calibration sample, which forms p–n junctions beneath the n-type stripes. We emphasize that under these electrical contact conditions, SSRM does not provide optimal sensitivity to carrier concentration and is likely influenced by contact-induced asymmetries, as evidenced by the differing responses for both polarities shown in Figure **5c**. Under the present analysis conditions, the large discrepancy between biasing configurations should be interpreted as the presence of an electronic junction in series with the region of interest beneath the n-type stripes. This junction introduces a substantial series resistance when reverse-biased, thereby contributing an additional resistance component to the overall SSRM resistance chain. An additional advantage of sMIM for dopant characterization is its ability to operate effectively without the need for an electrical back contact, a significant benefit for the analysis of fully processed device structures where such contacts are often inaccessible. Furthermore, as shown in Figures **6a** and **6b**, increasing the applied microwave power enhances the sensitivity of sMIM to doped features, consistent with its response to buried structures. While this approach is beneficial when a higher a.c. bias is either impractical or undesirable, excessive microwave power may lead to electronic saturation within the sMIM detection circuitry, as evidenced in Figure **6b**.

IV. DISCUSSION

A comprehensive understanding of the contrast mechanisms governing sMIM in relation to buried and doped features is of particular relevance to the semiconductor industry. The results presented in this work demonstrate that, unlike other scanning probe techniques such as C-AFM and SSRM, the sensitivity of sMIM is mainly independent of the applied tip–sample pressure. This effect, which is primarily dependent on the near-field coupling between tip and sample, results in a limited ability to tune the sampling volume under the tip-sample junction. Instead, the dynamic tuning of sensitivity is achieved through adjustment of the incident microwave power, which likely modifies the effective probing depth or the spatial extent of the microwave interaction volume, thereby enhancing the response of the MIM-C channel. Environmental conditions within the AFM chamber were also found to exert a pronounced influence on the overall sMIM sensitivity. Measurements conducted under high vacuum conditions demonstrated an increased dynamic range, yielding up to a 1.5x improvement in signal-to-noise ratio and thereby enhancing the detection of weakly contrasted features. Interestingly, subsequent reintroduction of ambient air further enhanced the dynamic range, suggesting that a complex interplay between residual surface water, adsorbate desorption, and tip–sample interface modifications may contribute to the observed improvement. The presence of a thin water layer has been shown to induce variations in electrostatic properties, for example, through screening effects, as well as to alter tip dynamics, which can in turn lead to changes in the measured signal and, consequently, image contrast.[34,35] Possible mechanisms underlying this behavior include enhanced microwave coupling efficiency, reduced parasitic capacitance pathways, or improved signal transmission through the tip–sample junction, which further work will have to establish. Beyond sensitivity, this study also provides insights into the spatial sampling of buried structures. The apparent underrepresentation of feature dimensions was found to increase with the depth of burial. Consequently, while the detection of deeply buried structures is feasible, accurate dimensional reconstruction may be limited. Despite these constraints, sMIM demonstrated a clear advantage for active dopant characterization compared to SCM and SSRM. This superiority arises from its larger effective probing volume, which yields an improved signal-to-noise ratio and reduces artifacts related to the sample's topography, and from its ability to operate without an electrical back contact, an essential capability for the analysis of fully fabricated or encapsulated transistor devices.

V. CONCLUSIONS

This study highlights the potential of microwave-based and near-field-assisted scanning probe methods as a powerful tool for electrical metrology and failure analysis in advanced semiconductor devices. By demonstrating its capability to probe both doped and buried structures without the need for an electrical back contact, sMIM addresses several limitations of conventional scanning probe techniques, which will be useful in combination with the three-dimensional features found in novel transistor devices, such as GAAFETs. Future work should aim to establish quantitative models linking sMIM signals to material and device parameters, as well as to develop standardized calibration procedures for complex geometries. Expanding the technique's applicability to fully fabricated devices and integrating it into industrial failure analysis workflows would represent key steps toward its broader adoption in semiconductor metrology.

SUPPLEMENTARY MATERIAL

See the supplementary material for more information on the sMIM-C dynamic range dependence on the variation of environmental conditions.

ACKNOWLEDGEMNTS

The authors acknowledge the help of Infineon Technologies AG, particularly Thomas Schweinböck, for providing their dopant calibration sample. The authors also acknowledge the assistance of facilities from the Eyring Materials Center at Arizona State University.

AUTHOR DECLARATIONS

Conflicts of Interest

The authors have no conflicts to disclose.

Ethics Approval

Ethics approval not required.

DATA AVAILABILITY

The data that support the findings of this study are available from the corresponding author upon reasonable request.

REFERENCES

1 N. G. Orji, M. Badaroglu, B. M. Barnes, C. Beitia, B. D. Bunday, U. Celano, R. J. Kline, M. Neisser, Y. Obeng, and A. E. Vladar, Nat Electron **1**, 532–547 (2018).
2 U. K. Das, and T. K. Bhattacharyya, IEEE Transactions on Electron Devices **67**, 2633–2638 (2020).
3 J. Ryckaert et al., *2018 IEEE Symposium on VLSI Technology* (2018), pp. 141–142.
4 C. Zhu, X. Zhu, S. Yu, and D. Wei Zhang, IEEE Access **13**, 21600–21609 (2025).
5 H. H. Radamson et al., Nanomaterials **14**, 837 (2024).
6 P. Favia et al., Semicond. Sci. Technol. **34**, 124003 (2019).
7 J. Bogdanowicz et al., Meet. Abstr. **MA2024-02**, 2302 (2024).
8 G. R. Muthinti et al., *Metrology, Inspection, and Process Control for Microlithography XXXII* (SPIE, 2018), p. 105850Z.
9 A.-L. Charley, H. Mertens, N. Horiguchi, P. Leray, N. Figueiró, M. Sendelbach, R. Koret, A. Ger, and S. Wolfling, *Metrology, Inspection, and Process Control for Microlithography XXXII* (SPIE, 2018), p. 1058505.
10 A. Tselev, IEEE Microwave Magazine **21**, 72–86 (2020).
11 R. C. Germanicus, P. D. Wolf, F. Lallemand, C. Bunel, S. Bardy, H. Murray, and U. Lüders, Beilstein J. Nanotechnol. **11**, 1764–1775 (2020).
12 D. Tami, D. A. A. Ohlberg, C. Gonçalves do Rego, G. Medeiros-Ribeiro, and J. C. Ramirez, APL Mater. **13**, 010602 (2025).
13 O. Amster, Y. Yang, B. Drevniok, S. Friedman, F. Stanke, and St. J. Dixon-Warren, *2017 IEEE 24th International Symposium on the Physical and Failure Analysis of Integrated Circuits (IPFA)* (2017), pp. 1–4.
14 G. Bargas, D. A. A. Ohlberg, K. Watanabe, T. Taniguchi, L. C. Campos, and G. Medeiros-Ribeiro, physica status solidi (b) **262**, 2400548 (2025).
15 D. A. A. Ohlberg et al., *Low-Dimensional Materials and Devices 2020* (SPIE, 2020), pp. 31–37.
16 K. A. Rubin, Y. Yang, O. Amster, D. A. Scrymgeour, and S. Misra, *Electrical Atomic Force Microscopy for Nanoelectronics*, edited by U. Celano (Springer International Publishing, Cham, 2019), pp. 385–408.
17 L. Wang, H. Chen, M. Chen, Y. Long, K. Liu, and K. P. Loh, Advanced Functional Materials **34**, 2316583 (2024).
18 R. Xu et al., Nanotechnology **30**, 205702 (2019).
19 A. Farokh Payam, and A. Passian, Science Advances **9**, eadg8292 (2023).
20 D. A. Scrymgeour, A. Baca, K. Fishgrab, R. J. Simonson, M. Marshall, E. Bussmann, C. Y. Nakakura, M. Anderson, and S. Misra, Applied Surface Science **423**, 1097–1102 (2017).
21 O. Amster, K. A. Rubin, Y. Yang, D. Iyer, and A. Messinger, Microelectronics Reliability **88–90**, 250–254 (2018).

22 O. Amster, K. Rubin, Y. Yang, D. Iyer, A. Messinger, and R. Crowder, *2018 IEEE International Symposium on the Physical and Failure Analysis of Integrated Circuits (IPFA)* (2018), pp. 1–5.
23 D. Iyer, A. Messinger, R. Crowder, Y. Zhang, O. Amster, S. Friedman, Y. Yang, and F. Stanke, (ASM International, 2017), pp. 613–617.
24 M. E. Barber, E. Y. Ma, and Z.-X. Shen, Nat Rev Phys **4**, 61–74 (2022).
25 Y. Yang, K. Lai, Q. Tang, W. Kundhikanjana, M. A. Kelly, K. Zhang, Z. Shen, and X. Li, J. Micromech. Microeng. **22**, 115040 (2012).
26 D. Goghero, V. Raineri, and F. Giannazzo, Appl. Phys. Lett. **81**, 1824–1826 (2002).
27 D. A. A. Ohlberg et al., Nat Commun **12**, 2980 (2021).
28 D. C. Lopez, D. A. A. Ohlberg, B. Giraldo, J. C. Ramirez, N. P. Kobayashi, C. G. do Rego, and G. Medeiros-Ribeiro, *Low-Dimensional Materials and Devices 2021* (SPIE, 2021), pp. 45–53.
29 E. Seabron, S. MacLaren, K. Jones, and W. L. Wilson, J. Appl. Phys. **125**, 174303 (2019).
30 X. Liu, X. Wang, X. Liu, Y. Song, Y. Zhang, H. Wang, Y. Zhang, G. Wang, and C. Zhao, Microelectronic Engineering **297**, 112310 (2025).
31 R. Coq Germanicus, M. Chaudhary, E. Vuillermet, and M. Lazar, *ISTFA 2025: Proceedings from the 51st International Symposium for Testing and Failure Analysis* (ASM International, 2025), pp. 404–410.
32 J. Smoliner, B. Basnar, S. Golka, E. Gornik, B. Löffler, M. Schatzmayr, and H. Enichlmair, Appl. Phys. Lett. **79**, 3182–3184 (2001).
33 F. Giannazzo, D. Goghero, and V. Raineri, J. Vac. Sci. Technol. B **22**, 2391–2397 (2004).
34 N. Nakagiri, H. Sugimura, Y. Ishida, K. Hayashi, and O. Takai, Surface Science **532–535**, 999–1003 (2003).
35 S. Santos, and A. Verdaguer, Materials **9**, 182 (2016).